RSC Advances

PAPER

View Article Online
View Journal | View Issue

Cite this: *RSC Adv.*, 2018, **8**, 41749

Self-assembled hierarchical porous $NiMn_2O_4$ microspheres as high performance Li-ion battery anodes†

Shuang Zhao, Honglei Li, Zhixu Jian, Yalan Xing* and Shichao Zhang*

Received 29th September 2018
Accepted 2nd December 2018

DOI: 10.1039/c8ra08080a

rsc.li/rsc-advances

Hierarchical structured porous $NiMn_2O_4$ microspheres assembled with nanorods are synthesized through a simple hydrothermal method followed by calcination in air. As anode materials for lithium ion batteries (LIBs), the $NiMn_2O_4$ microspheres exhibit a high specific capacity. The initial discharge capacity is 1126 mA h g^{-1}. After 1000 cycles, the $NiMn_2O_4$ demonstrates a reversible capacity of 900 mA h g^{-1} at a current density of 500 mA g^{-1}. In particular, the porous $NiMn_2O_4$ microspheres still could deliver a remarkable discharge capacity of 490 mA h g^{-1} even at a high current density of 2 A g^{-1}, indicating their potential application in Li-ion batteries. This excellent electrochemical performance is ascribed to the unique hierarchical porous structure which can provide sufficient contact for the transfer of Li^+ ion and area for the volume change of the electrolyte leading to enhanced Li^+ mobility.

Introduction

The development of sustainable new energy sources is considered as a feasible solution to solve the energy crisis and global environmental pollution.[1–3] Lithium-ion batteries (LIBs) with high power density, high output voltage and low environmental pollution, show superior performance to traditional secondary batteries and have been widely used in portable mobile electronic devices and power vehicles.[4–7] However, the specific capacity of current commercial lithium-ion batteries is still stuck at a low level and fail to satisfy the demands of large-scale applications. Therefore, it is necessary to develop new electrode materials with high reversible specific capacity, high rate performance and long cycle life to meet the greater demand for high energy density LIBs.[8–12]

Compared with traditional graphite anode materials, transition metal oxides (TMOs) have higher theoretical specific capacity (700–900 mA h g^{-1}) and better specific power characteristics, which can meet the energy density needs of power batteries.[13,14] Moreover, owing to their lower voltage and higher energy density, binary manganese-based composite metal oxide anode materials such as $ZnMn_2O_4$, $NiMn_2O_4$, and $CoMn_2O_4$ have attracted enormous attention.[15–18] Wang *et al.* fabricated a novel $ZnMn_2O_4$/N-doped graphene (ZMO/NG) nanohybrid with a sandwiched structure which exhibits a specific capacity of 747 mA h g^{-1} after 200 cycles at 500 mA g^{-1}.[19] Zhang *et al.* obtained pure phase $ZnMn_2O_4$ samples sandwiched *via* a combustion assisted coprecipitation method with a specific capacity of 716 mA h g^{-1} after 90 cycles at 100 mA g^{-1}.[20] Hu *et al.* fabricated the spinel $CoMn_2O_4$ hierarchical mesoporous microspheres with a specific capacity of 894 mA h g^{-1} after 65 cycles at 100 mA g^{-1}.[21] Wang and his team developed a $NiMn_2O_4$/C array of sandwich structures on Ni foil by a simple hydrothermal reaction, and obtained a $NiMn_2O_4$ composite with excellent performance as a negative electrode of a lithium ion battery at a current density of 500 mA g^{-1}. After 200 cycles, the ultra-high specific capacity of 1346 mA h g^{-1} was maintained.[22] Ma *et al.* obtained a superior $NiMn_2O_4$ based anode material by incorporating Fe into $NiMn_2O_4$, and maintained 620 mA h g^{-1} after circulating 250 times at a current density of 200 mA g^{-1} as the negative electrode for a lithium ion battery.[23]

Among the manganese-based binary oxides, spinel-structured $NiMn_2O_4$ with the advantages of abundant resources and environmental benignancy shows potential commercial application in Li-ion batteries.[24] Moreover, the synergistic effects of Ni^{2+} and Mn^{3+} during cycling also provide a high specific capacity (922 mA h g^{-1}), and the electrochemical reaction of the $NiMn_2O_4$ electrode is as follows:[25–28]

$$NiMn_2O_4 + 8Li^+ + 8e^- \rightarrow Ni + 2Mn + 4Li_2O \quad (1)$$

$$Ni + Li_2O \rightarrow NiO + 2Li^+ + 2e^- \quad (2)$$

$$Mn + Li_2O \rightarrow MnO + 2Li^+ + 2e^- \quad (3)$$

$$2MnO + 1/3Li_2O \rightarrow 1/3Mn_3O_4 + 3Li^+ + 2/3e^- \quad (4)$$

Although the $NiMn_2O_4$ electrode material has so many advantages, it still possesses poor conductivity and large

School of Materials Science and Engineering, Beihang University, Beijing 100191, PR China. E-mail: csc@buaa.edu.cn; Fax: +86 01082338148; Tel: +86 01082339319

† Electronic supplementary information (ESI) available. See DOI: 10.1039/c8ra08080a

volume changes during the charging and discharging processes as an anode material for LIBs.[29,30] The insertion/extraction of lithium ions generates huge volume changes during cycling which lead to serious pulverization and agglomeration of the anode materials and reduce the contact area between the active material and the electrolyte. Thus, the design of $NiMn_2O_4$ oxides with a unique hierarchical porous structure are considered to be essential to mitigate the volume change and to solve the above problems.

Herein, we first synthesized novel hierarchical porous $NiMn_2O_4$ microspheres by a one-step hydrothermal reaction and subsequent heat treatment with KMn_2O_4 as the manganese source. As a LIB anode material, the $NiMn_2O_4$ microspheres exhibit a high specific capacity. The initial discharge capacity is 1126 mA h g^{-1} and after 1000 cycles, the specific capacity is 900 mA h g^{-1}. In particular, the porous $NiMn_2O_4$ microspheres could still deliver a remarkable discharge capacity of 490 mA h g^{-1} even at a high current density of 2 A g^{-1}, indicating considerable potential application in high energy density Li-ion batteries.

Results and discussion

The Ni–Mn precursor was obtained with the simple hydrothermal method. The bottom curve of Fig. 1a shows XRD patterns of the Ni–Mn precursor. It can be seen that the precursor's crystallinity is poor and the diffraction peaks are not correspond to any nickel or manganese compound. It indicates that the precursor is not a spinel-type $NiMn_2O_4$. Heat treatment is necessary to obtain spinel-type $NiMn_2O_4$. The DTG/TG (Fig. 1b) analysis of the precursor (under an air atmosphere) shows that the precursor has two distinct exothermic peaks at 500 °C and 790 °C with the weight reduction. According to the curve, it can be inferred that some exothermic reaction occurs in the vicinity of these two temperatures, corresponding to the formation or transformation of the crystal structure. Therefore, the precursor was calcined at 600 and 800 °C in an air atmosphere to obtain the products NMO-600 and NMO-800. XRD (Fig. 1a) analysis proves that NMO-600 contains a variety of nickel–manganese oxides, such as $NiMnO_3$ (JCPDS 65-3695), MnO_2 (JCPDS 44-0141) *etc.*; while the diffraction peak of NMO-800 corresponds to the peak on the standard card of $NiMn_2O_4$ (JCPDS 36-0083). It indicates that the precursor can be converted to $NiMn_2O_4$ at a calcination temperature of 800 °C, but not at 600 °C. Therefore, the exothermic peak and mass drop at 790 °C on the DSC/TG curve correspond to the formation of spinel structure, while the peak near 500 °C corresponds to the transformation of multiphase material, but fails to form a spinel structure $NiMn_2O_4$.

Fig. 2 displays the SEM image of the precursor and NMO-800. Fig. S1† shows the SEM image of the NMO-600. It can be seen that the precursor and the NMO-600 have the hierarchical porous microsphere structure, the NMO-800 are hierarchical porous microspheres composed of nanorods with a diameter in the range of 4–5 μm. The elemental mapping of O, Mn and Ni depicted in Fig. 2c shows the uniform distribution of all elements in the microspheres. The structure will provide space for volume expansion during deintercalation of lithium and increase the contact area between the electrode and the electrolyte. Meanwhile, the nanorods will shorten the diffusion distance of lithium ions in the active material and improve its conductivity. The hierarchical porous microsphere structure of NMO-800 was further confirmed by the TEM observation. Moreover, the TEM image (Fig. 3a) indicates that the interior of the microspheres is also porous. The HRTEM image (Fig. 3b) shows that the lattice fringe spacing is 0.485 nm, which corresponds to the (111) plane of the spinel $NiMn_2O_4$ phase. The uniformity of lattice fringes indicates that the porous $NiMn_2O_4$ microsphere has a high crystallinity. The oxidation state of the corresponding transition metal ions in the obtained sample was further investigated by X-ray photoelectron spectroscopy (XPS). The survey spectrum (Fig. 4a) confirms the presence of Ni, Mn and O elements and the C 1s (284.79 eV) peak is used as a standard peak. By magnifying the area corresponding to each element, we further understand the atomic state of each element in NMO-800. The Ni 2p spectrum is shown in Fig. 4b, and the three peaks in the spectrum are $2p_{1/2}$, $2p_{3/2}$, and the satellite peaks of $2p_{3/2}$ of Ni atoms, respectively. Among them, the difference of $2p_{3/2}$ and its satellite peaks characterizes the degree of electron hybridization of p orbital and 3d orbital in Ni atom, and the difference of 6.77 eV indicates that Ni element exists in divalent form.[31] In the Mn 2p spectrum (Fig. 4c), the two peaks located at 653.5 eV and 641.8 eV are correspond to the Mn $2p_{1/2}$ and Mn $2p_{3/2}$ orbitals, respectively, with the difference

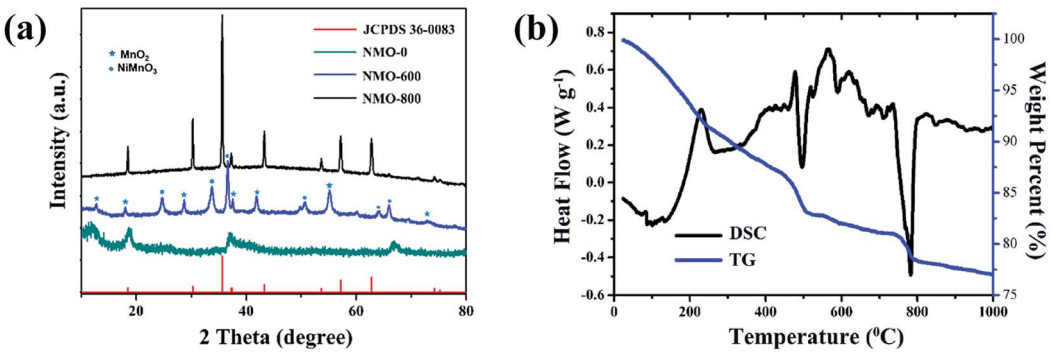

Fig. 1 (a) The XRD pattern of the as-prepared NMO-0, NMO-600, and ZMO-800. (b) DSC/TG curve of the precursor of Ni–Mn.

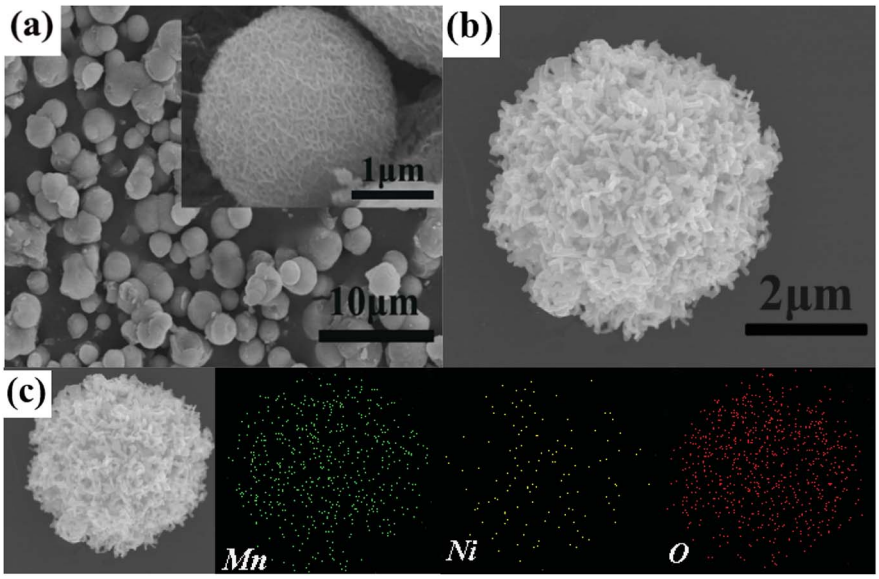

Fig. 2 SEM images of (a) NMO-0, (b) NMO-800 and (c) the elemental mapping of Ni, Mn and O of NMO-800.

of 11.7 eV, which is consistent with the previous literature. It indicates that the Mn element exists in the form of trivalent. The O 1s (Fig. 4d) which have been splitted into two different valence states: one peak at 529.7 eV is due to the typical metal–oxygen bonds, while the other broad peaks at 529–533 eV are due to the lattice oxygen in the spinel $NiMn_2O_4$ (530.8 eV) and the surface adsorbed oxygen (531.8 eV).[32,33]

The nitrogen desorption experiment was used to characterize the specific surface area and the pores size distribution, the results are shown in Fig. 5. The BET results indicate that it has a specific surface area of 15.6 $m^2\ g^{-1}$ and a specific pore volume of 0.044 $cm^3\ g^{-1}$; the BJH pore size distribution indicates that the pore size is mainly concentrated at 2 to 50 nm. These pore structures will provide a buffer space for the volume expansion of the electrode during charge and discharge, and increase the contact area between the electrolyte and the active material, thereby reducing the lithium ion diffusion distance and improving its cycle performance and rate performance.

The electrochemical performance of the NMO-800 as anode materials for LIBs was investigated by cyclic voltammetry (CV). The results are shown in Fig. 6a, including cyclic voltammetry curves of the 1st, 2nd, and 10th. In the first cycle, there are three peaks. The broad peak centered at 1.3 V, which can be attributed to the reduction of Mn^{3+} to Mn^{2+}. The reduction peak located at ~0.70 V is ascribed to the reduction of Ni^{2+} to Ni, and may along with the formation of solid electrolyte interface film; the reduction peak located at ~0.25 V is ascribed to the reduction of Mn^{2+} to Mn.

The three reduction reactions of the first cycle is accompanied by the lithium-ion embedding to form Li_2O and the formation Ni and Mn metal. There are two oxidation peaks at 1.26 V and 1.92 V, respectively. The broad oxidation peak at ~1.26 V is ascribed to the oxidation of Mn to MnO, accompanied by desorption of Li^+; the relatively sharp oxidation peak at ~1.92 V is ascribed to the oxidation of Ni to NiO, accompanied by the desorption of Li^+. The delithiation potential of the negative electrode directly affects the output voltage of the lithium ion battery, thereby affecting its energy density. The higher the negative electrode potential, the lower the energy density. The delithiation potential of NiO as a negative electrode of a lithium ion battery is about 2.3 V. In comparison, the delithiation potential of about 1.92 V of NiO formed in NMO-800 clearly means a higher energy density.[34] In the following cycles, the reduction peak near 1.5 V in the first cycle

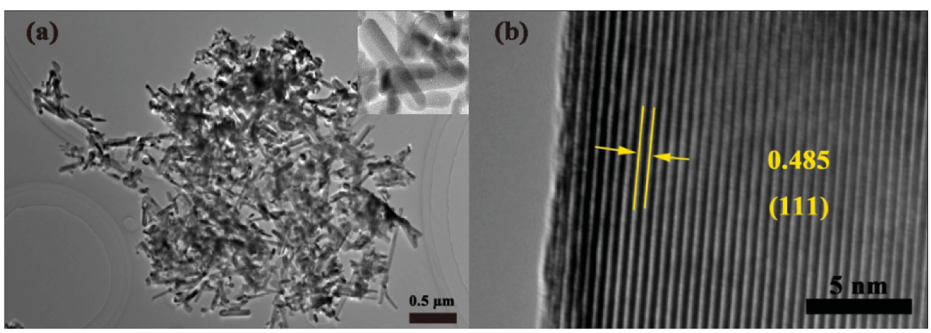

Fig. 3 (a) TEM images of NMO-800, (b) HRTEM images of NMO-800.

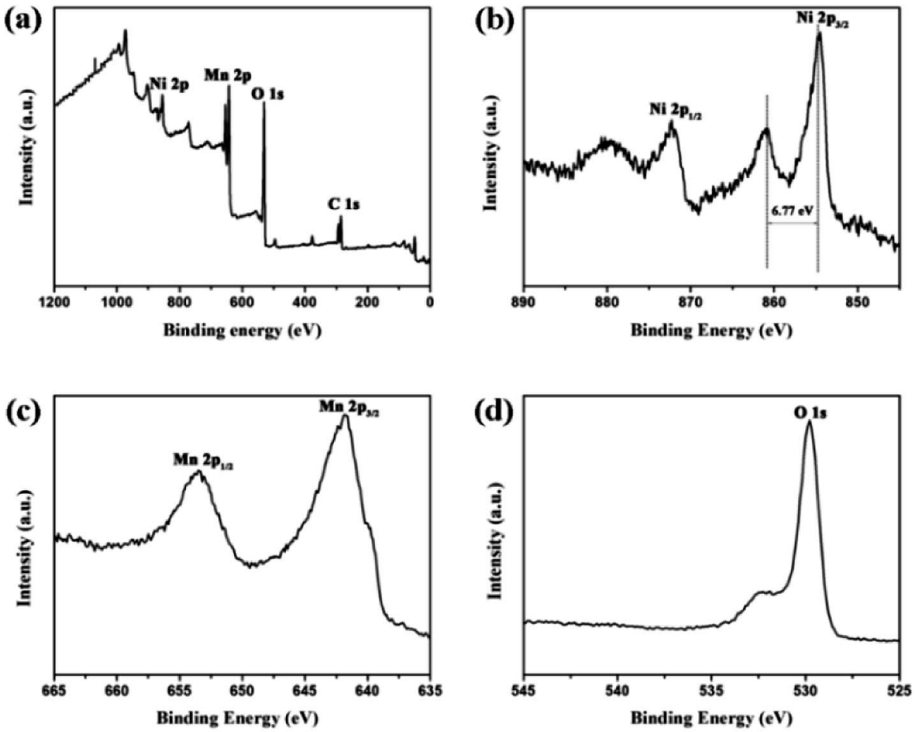

Fig. 4 XPS spectra of ZMO-500: survey spectrum (a); Ni 2p (b); Mn 2p (c) O 1s (d).

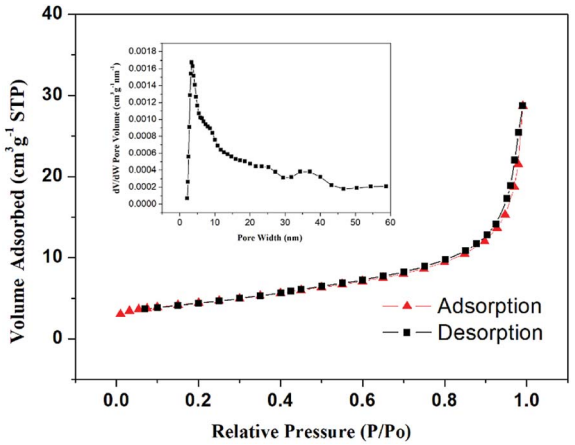

Fig. 5 N_2 adsorption/desorption isotherm and corresponding pore size distribution of NMO-800.

disappears, because of the disappearance of Mn^{3+}, while the other redox peaks are coincide with the peak position of the first cycle, indicating that NMO-800 has good cycle stability. Based on the above CV analysis, we confirmed the electrochemical reactions for the $NiMn_2O_4$ electrode as a negative electrode of a lithium ion battery.

Fig. 6b shows the typical charge and discharge curves of NMO-800 at a current density of 500 mA h g^{-1} between 0.01–3.0 V. In the first discharge process, the voltage plateau at about 0.70 V and 0.25 V, which are consistent with the CV curve and corresponds to the reduction of NiO and MnO, respectively. The initial discharge capacity is 1126 mA h g^{-1} with a coulombic efficiency (CE) of 74%. The extra capacity could be attributed to the irreversible capacity originated from the decomposition of the solvent in the electrolyte solution and the formation of a solid electrolyte interphase (SEI) layer.[22,35] And the capacity lost is attributed to the formation of solid electrolyte interface film (SEI).

As shown in Fig. 6c, at the subsequent charge and discharge cycles, the coulombic efficiency begins to rise, but its specific capacity decreases rapidly. Until to the 40th cycle, it has dropped to 460 mA h g^{-1}. The specific capacity eventually stabilize around the 600th cycle, which reaches above 900 mA h g^{-1}. This phenomenon may be mainly due to the activation mechanism of the electrode during the cycles. First, the SEI film is continuously formed on the new surfaces generated by the volume change, which could affect the lithium storage and lead to capacity fading at an early stage. After the further charging and discharging, the structure of binary metal oxides are reconstructed with SEI films tending to be stable, and the electrolyte gradually penetrates into the inner part of the active materials, which contribute to the increased charge–discharge capacity and superior cycle performance.[33,36] After 1000 cycles, the capacity reaches a stable capacity of 900 mA h g^{-1}, which is close to the theoretical specific capacity of $NiMn_2O_4$, indicating that the active material of NMO-800 is almost not destroyed during the cycles. This may be attributed to the hierarchical porous structure and the mutual support between Ni, Mn and their oxides formed after the cycles, which together alleviate the volume change of the metal oxide during charge and discharge process, thus the protective electrode is not destroyed. Fig. S2† shows the cycling performance of NMO-600 at a current density

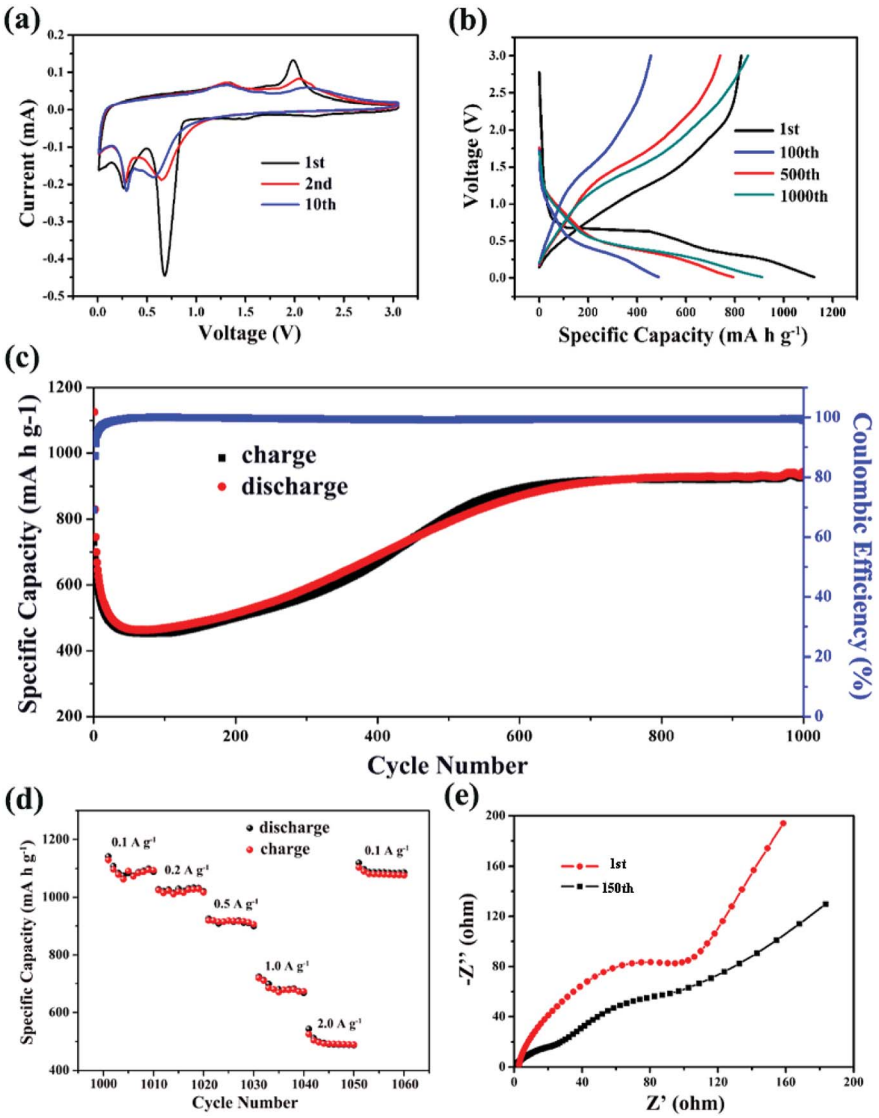

Fig. 6 CV curves of the NMO-800 electrode in the voltage range of 0.01–3.0 V at a scan rate 0.1 mV s^{-1} (a); discharge–charge curves of the NMO-800 electrode at the current density of 500 mA g^{-1} (b); cycling performance of NMO-800 at a current density of 500 mA g^{-1} (c) and rate performance at various current densities from 100 to 2000 mA g^{-1} (d); EIS of the $NiMn_2O_4$ electrode (e).

of 500 mA g^{-1}. It can be seen that the stable specific capacity is about 600 mA h g^{-1} which is less than NMO-800, indicating that NM0-800 has an excellent performance.

Fig. 6d shows the cycling behavior of the as-prepared NMO-800 at different current densities of 0.1, 0.2, 0.5, 1.0, 2.0, 0.1 A g^{-1}. The specific capacity changes from 1090 mA h g^{-1} to 490 mA h g^{-1}. Finally the specific capacity revert to above 1000 mA h g^{-1}, which indicates a good rate cycling. The above results prove that NMO-800 has excellent rate performance and structural stability.

In order to investigate the conductivity of the NMO-800 electrode, we conducted an AC impedance test. The Nyquist plot is shown in Fig. 6e. The figure shows the Nyquist curve of NMO after the first and the 150th cycle. At the first cycle, the semicircle of the high frequency region represents the charge transfer resistance of the electrode, and the oblique line of the low frequency region is related to the diffusion of lithium ions in the electrode. It can be seen that the NMO-800 electrode has a small charge transfer resistance, which may be due to the NMO-800's nano composition. The NMO-800's surface is activated because of nano effect, so that the charge is easy to transfer. Through further analysis, we find that the charge transfer resistance of the electrode after the 150th cycle is smaller than that the first cycle, which may be attributed to the change of the electrode active material after the charge and discharge, resulting in the change of the structure and the electrode surface state with the electrode electrochemical activated.[26]

Conclusions

Hierarchical porous $NiMn_2O_4$ microspheres are synthesized through a simple hydrothermal method and subsequent calcination with a new manganese source ($KMnO_4$). The structure

will provide space for volume expansion during deintercalation of lithium and increase the contact area between the electrode and the electrolyte. At the same time, the nanorods will shorten the diffusion distance of lithium ions in the active material and improve its conductivity. Therefore NMO-800 shows a high specific capacity of 900 mA h g^{-1} retained after 600 cycles at 500 mA g^{-1} and a good rate performance. The hierarchical porous material could be coated with carbon to further improve the performance of the material and be promising to be used as an anode for next generation LIBs.

Experimental

Preparation of materials

Fabrication of the NMO-800 microspheres. 1 mmol of zinc chloride ($NiCl_2$), 2 mmol of potassium permanganate ($KMnO_4$) and 2 mmol of sodium fluoride (NaF) were dissolved in 100 mL of deionized water to form a purple solution under the magnetic stirring until the solution was stirred uniformly. The solution was then transferred to a 100 mL Teflon-lined stainless steel autoclave, which was then placed in an oven and held at 200 °C for 24 hours. After cooling to room temperature, the precursor precipitate was washed several times through a vacuum suction device using deionized water, followed by oven drying at 60 °C overnight. In order to obtain the final product $NiMn_2O_4$, the above dried precipitates were calcined in air at a heating rate of 2 °C min^{-1} for 2 h at two different temperatures of 600, 800, respectively, to obtain four different products, denoted as NMO-600 and NMO-800, respectively.

Structural and morphological characterization

Differential scanning calorimetry thermogravimetric (DSC/TG) curves were obtained in air at a heating rate of 10 °C min^{-1} using a NETZSCH STA 449C thermal analyzer. The crystal phase composition of the product was analyzed by X-ray diffraction (XRD, Rigaku D/Max-2400) with an energy dispersive spectrometer (EDS) using CuKα radiation. Transmission electron microscopy (TEM, JEM-2100F), and high resolution transmission electron microscopy (HR-TEM, FEI, Tecnai G2 F20). And the atomic information in the crystal was collected to X-ray photoelectron spectroscopy (XPS, Thermo VG ESCALAB 250), Raman microscope (voltage: 100–240 V, power: 150 W; RENISHAW Invia, UK), BET surface-area and pore-size analyzer (Quantachrome Autosorb-6B).

Cell assembly and electrochemical measurements

Preparation of the disc. The obtained $NiMn_2O_4$, conductive carbon black and polyvinylidene fluoride (PVDF) binder were uniformly mixed in a ratio of 8 : 1 : 1, and after fully grinding in the mortar, the powder is transferred to a small weighing bottle and was stirred with the solvent *N*-methylpyrrolidone (NMP) for 30 minutes to obtain a slurry, and the slurry was uniformly coated on a copper foil. It was then dried under vacuum at 80 °C for 12 hours. Finally, the copper foil coated with the active material was cut into a disc with a diameter of 1 cm.

Coin cell assembly. A coin cell (CR2032) was assembled in an argon-filled glovebox with as-prepared electrode as the anode and lithium foil (Sigma-Aldrich) as the counter electrode and the reference electrode. The anode and cathode were separated by a Celgard 2400 separator and a 1 M $LiPF_6$ electrolyte of ethylene carbonate (EC)-dimethyl carbonate (DMC) (EC/DMC = 1 : 1, by volume). The battery was discharged and charged using a NWEARE BTS-610 tester, and a cyclic voltammetry (CV) test was performed using a CHI 660D electrochemical workstation at a scan rate of 0.1 mV s^{-1}, both having a potential range of 0.01–3.0 V *vs.* Li^+/Li. Electrochemical impedance spectroscopy (EIS) was performed at the open circuit voltage by the Zahner IM6e electrochemical workstation, and the frequency range of the electrochemical workstation ranges from 10 MHz to 10 mHz. All of the above electrochemical tests were carried out at room temperature.

Conflicts of interest

There are no conflicts to declare.

Acknowledgements

This work was supported by National Natural Science Foundation of China (51575030 and 51774017), Beijing Natural Science Foundation (2174075), Key Program of Equipment Pre-Research Foundation of China (6140721020103) and Scientific Research Foundation of SGCC (52170217000L).

Notes and references

1 K. Amine, R. Kanno and Y. Tzeng, *MRS Bull.*, 2014, **39**, 395–401.
2 J. B. Goodenough and Y. Kim, *J. Power Sources*, 2011, **196**, 6688–6694.
3 J. Xu, S. Dou, H. Liu and L. Dai, *Nano Energy*, 2013, **2**, 439–442.
4 J. B. Goodenough and Y. Kim, *Chem. Mater.*, 2010, **22**, 587–603.
5 D. Andre, S. J. Kim, P. Lamp, S. F. Lux, F. Maglia, O. Paschos and B. Stiaszny, *J. Mater. Chem. A*, 2015, **3**, 6709–6732.
6 D. Larcher and J. Tarascon, *Nat. Chem.*, 2015, **7**, 19–29.
7 J. R. Croy, A. Abouimrane and Z. Zhang, *MRS Bull.*, 2014, **39**, 407–415.
8 G. B. Peter, S. Bruno and T. Jean-Marie, *Angew. Chem., Int. Ed.*, 2008, **47**, 2930–2946.
9 Y. G. Guo, J. S. Hu and L. J. Wan, *Adv. Mater.*, 2010, **20**, 2878–2887.
10 M. Armand and J. M. Tarascon, *Nature*, 2008, **451**, 652–657.
11 Y. Idota, T. Kubota, A. Matsufuji, Y. Maekawa and T. Miyasaka, *Science*, 1997, **276**, 1395–1397.
12 J. M. Tarascon and M. Armand, *Nature*, 2001, **414**, 359–367.
13 A. G. Belous, O. Z. Yanchevskii and A. V. Kramarenko, *Russ. J. Appl. Chem.*, 2006, **79**, 345–350.
14 R. Holze, *J. Solid State Electrochem.*, 2005, **9**, 794–795.
15 Y. L. Ding, X. B. Zhao, J. Xie, G. S. Cao, T. J. Zhu, H. M. Yu and C. Y. Sun, *J. Mater. Chem.*, 2011, **21**, 9475–9479.

16 d. K. Kim, P. Muralidharan, H. W. Lee, R. Ruffo, Y. Yang, C. K. Chan, H. Peng, R. A. Huggins and Y. Cui, *Nano Lett.*, 2008, **8**, 3948–3952.
17 L. Zhou, H. B. Wu, T. Zhu and X. W. Lou, *J. Mater. Chem.*, 2011, **22**, 827–829.
18 X. Zhang, F. Cheng, K. Zhang, Y. Liang, S. Yang, J. Liang and J. Chen, *RSC Adv.*, 2012, **2**, 5669–5675.
19 D. Wang, W. Zhou, Y. Zhang, Y. Wang, G. Wu, K. Yu and G. Wen, *Nanotechnology*, 2016, **27**, 045405.
20 T. Zhang, Y. Gao, H. Yue, H. Qiu, Z. Guo, Y. Wei, C. Wang, G. Chen and D. Zhang, *Electrochim. Acta*, 2016, **198**, 84–90.
21 L. Hu, H. Zhong, X. Zheng, Y. Huang, P. Zhang and Q. Chen, *Sci. Rep.*, 2012, **2**, 986.
22 Y. Ouyang, Y. Feng, H. Zhang, L. Liu and Y. Wang, *ACS Sustainable Chem. Eng.*, 2016, **5**, 196–205.
23 Y. Ma, C. W. Tai, R. Younesi, T. Gustafsson, J. Y. Lee and K. Edström, *Chem. Mater.*, 2015, **27**, 7698–7709.
24 F. Courtel, H. Duncan, Y. Abulebdeh and I. Davidson, *J. Mater. Chem.*, 2011, **21**, 10206–10218.
25 Y. Ouyang, Y. Feng, H. Zhang, L. Liu and Y. Wang, *ACS Sustainable Chem. Eng.*, 2016, **5**, 196–205.
26 W. Kang, Y. Tang, W. Li, X. Yang, H. Xue, Q. Yang and C. S. Lee, *Nanoscale*, 2014, **7**, 225–231.
27 J. Li, S. Xiong, X. Li and Y. Qian, *Nanoscale*, 2013, **5**, 2045–2054.
28 L. Li, Y. Cheah, Y. Ko, P. Teh, G. Wee, C. Wong, S. Peng and M. Srinivasan, *J. Mater. Chem. A*, 2013, **1**, 10935–10941.
29 R. B. Rakhi, W. Chen, D. Cha and H. N. Alshareef, *Nano Lett.*, 2012, **12**, 2559–2567.
30 C. Yuan, H. B. Wu, Y. Xie and X. W. Lou, *Angew. Chem., Int. Ed.*, 2014, **53**, 1488–1504.
31 A. J. F. Cabral, J. P. Serna, B. R. Salles, M. A. Novak, A. L. Pinto and C. M. R. Remédios, *J. Alloys Compd.*, 2015, **630**, 74–77.
32 J. G. Kim, S. H. Lee, Y. Kim and W. B. Kim, *ACS Appl. Mater. Interfaces*, 2013, **5**, 11321–11328.
33 H. Sun, G. Xin, T. Hu, M. Yu, D. Shao, X. Sun and J. Lian, *Nat. Commun.*, 2014, **5**, 4526.
34 X. H. Huang, J. P. Tu, C. Q. Zhang and F. Zhou, *Electrochim. Acta*, 2010, **55**, 8981–8985.
35 W. Kang, Y. Tang, W. Li, X. Yang, H. Xue, Q. Yang and C. S. Lee, *Nanoscale*, 2015, **7**, 225–231.
36 F. Wu, S. Xiong, Y. Qian and S. H. Yu, *Angew. Chem., Int. Ed.*, 2015, **54**, 10787–10791.